

Joint Inversion of receiver functions and apparent incidence angles to determine the crustal structure of Mars

Rakshit Joshi^{1,5}, Brigitte Knapmeyer-Endrun², Klaus Mosegaard³, M. A. Wieczorek⁴, Heiner Igel⁵, Ulrich R. Christensen¹, Philippe Lognonné⁶

¹Max Planck Institute for Solar System Research, Göttingen, Germany

²Bensberg Observatory, University of Cologne, Cologne, Germany

³Niels Bohr Institute, University of Copenhagen, Copenhagen, Denmark

⁴Université Côte d'Azur, Observatoire de la Côte d'Azur, CNRS, Laboratoire Lagrange, Nice, France

⁵Ludwig-Maximilians-Universität, Munich, Germany

⁶Université de Paris, Institut de Physique du Globe de Paris, CNRS, Paris, France

Key Points:

- We apply recent results from random matrix theory to identify crustal phases in noisy receiver functions for Mars from InSight data
- Once identified, we jointly invert these phases with frequency-dependent apparent S-wave velocity curves
- Results show a crustal thickness of 43 km with two inter-crustal discontinuities at 8.5 km and 22 km beneath the lander

Abstract

Recent estimates of the crustal thickness of Mars show a bimodal result of either ~ 20 km or ~ 40 km beneath the InSight lander. We propose an approach based on random matrix theory applied to receiver functions to further constrain the subsurface structure. Assuming a spiked covariance model for our data, we first use the phase transition properties of the singular value spectrum of random matrices to detect coherent arrivals in the waveforms. Examples from terrestrial data show how the method works in different scenarios. We identify three new converted arrivals in the InSight data, including the second multiply reflected phase from a deeper third interface. We then use this information to jointly invert receiver functions with the absolute S-wave velocity information in the polarization of body waves. Results show a crustal thickness of 43 ± 5 km beneath the lander with two mid-crustal interfaces at depths of 8.5 ± 1.5 km and 22 ± 3 km.

1 Introduction

The InSight mission landed in the Elysium Planitia plain of Mars on November 26, 2018 (Banerdt et al., 2020) and deployed a 3 component very broadband seismometer (SEIS) (Lognonné et al., 2019, 2020) on the surface. Along with measuring the seismicity and the present thermal state of its interior, a primary goal of the mission is to constrain the interior structure of Mars. In comparison with the Earth, Mars has a relatively lower seismicity rate with quakes of smaller magnitude ($2\text{--}5 M_w$) (Giardini et al., 2020). Receiver function (RF) analysis is a robust single station technique that can be used in this case to constrain the crustal structure. Primary body waves (P and S) give rise to converted secondary phases (Ps and Sp) when they impinge upon a seismic discontinuity from beneath. RFs exploit these converted phases to gain information about the discontinuities in the crust and upper mantle. They have previously been used to investigate the thickness of the lunar crust using seismic data from the Apollo mission (Vinnik et al., 2001; Lognonné et al., 2003; Gagnepain-Beyneix et al., 2006). Using the data from the InSight mission, Lognonné et al. (2020) computed RFs from two marsquakes and showed evidence of subsurface layering with low seismic velocities in the first upper 8–11 km. Recently, Knapmeyer-Endrun et al. (2021) used RFs from three marsquakes and showed the observations to be consistent with either a two-layer model with the Moho at 20 ± 5 km or a three-layer model with the Moho at 39 ± 8 km depth below the lander. Although the thicker model is more compatible with geodynamical constraints, this ambiguity could not be resolved from the data due to a lack of phase move-out information and excessive noise in the later part (> 10 s) of the waveforms which inhibited the identification of multiply reflected arrivals. Compaire et al. (2021) and Schimmel et al. (2021) analyzed ambient field autocorrelations and identified reflection signals consistent with the first two interfaces. Li et al. (2022) confirmed the first interface at ~ 8 km depth and the anisotropic nature of the layer above based on SH-wave reflections. Kim et al. (2021) and Durán et al. (2022) later used updated RF datasets with more events to provide additional constraints and connoted a preference for the three-layer crustal model. Khan et al. (2021) and Drilleau et al. (2022) arrived at similar results using body wave travel-times. In this paper, we build upon the previous work of Knapmeyer-Endrun et al. (2021) to infer further constraints on the crustal structure of Mars using new techniques and additional data from the InSight mission.

We first focus on the problem of detection of multiply reflected phases in our selected RF dataset. For this, we propose a method that utilises recent results from the random matrix theory to extract coherent signals in the RF waveforms. Assuming the observed signal to be a superposition of random noise and an underlying low-rank signal, the eigenvalues of the data covariance matrix follow a well behaved and deterministic limiting spectral distribution dictated by the generalized Marchenko-Pastur law. This information can be effectively used to decouple and identify coherent signal eigenvalues reflecting primary subsurface features from a bulk spectrum formed by incoherent scattering, random noise, and small-scale

heterogeneity with distinct eigenvector rotation properties. Once identified, the secondary phase arrivals together with the primary conversions from crustal interfaces can be used to invert for the structure. We then address the problem of non-uniqueness of RF inversions. Being primarily sensitive to shear velocity contrasts of interfaces and relative travel-time of converted waves, inversions of RF data alone can be affected by depth velocity trade-off (Ammon, 1991). They are therefore usually inverted jointly with other independent data sets that provide additional constraints on absolute shear wave velocities like surface-wave dispersion (e.g. Du & Foulger (1999); Julia et al. (2000); Bodin et al. (2012)). Svenningsen & Jacobsen (2007) showed that P-wave polarization can also be used to constrain the S-wave velocity structure of the subsurface using a simple relation between the observed apparent incidence angle and half-space S-wave velocity (Wiechert, 1907). Following this, we previously showed how a joint inversion of apparent velocity curves and receiver function data can lead to a well constrained velocity structure for limited data sets comprising only a few events (Joshi et al., 2021). We adopt a similar methodology here to jointly invert an RF dataset with a mean apparent velocity curve using a transdimensional approach.

2 Data and Method

2.1 RF processing

InSight has identified 1244 marsquakes (InSight Marsquake Service, 2022) since its operations started in 2018. Each quake is assigned a type and quality depending on its energy content and uncertainty in location estimate (Giardini et al., 2020). Only a few of these propagate through the mantle like teleseismic earthquakes, most of which do not have a precise location. Our database for Mars thus consists of 8 LF and BB seismic events (InSight Mars SEIS Data Service, 2019) with high SNR and event quality A-B (Clinton et al., 2021). Details of the events used in this study are provided in the supplementary material. Most of these events have similar distances and back-azimuths as they all originate in the Cerberus Fosse region which is a young tectonic structure located to the east of the lander. S0183a is located farther away but we nevertheless use it as its inclusion does not have a significant effect on the results. For the terrestrial example, we use data from seismic station VSU in Vasula, Estonia. We select events with similar back-azimuth and distance range to mimic the InSight data.

To calculate RFs, we apply a time-domain Wiener filter for deconvolution as described by Hannemann et al. (2017). We first remove the transfer functions from the individual components of the data, rotate to ZNE coordinates as VBB uses the U, V, W component system, and filter the seismograms between the corner frequencies (listed in supplementary materials) using a zero-phase Butterworth filter. Subsequently, the ZNE coordinate system is rotated into ZRT to obtain radial and transverse components using the back-azimuth estimates provided by MQS. A Wiener filter is determined such that it transforms the P-wave signal on the vertical component into a band-limited spike. All the components of the data are then folded with this filter to obtain the RFs. The terrestrial data was processed similarly but was filtered between 5 Hz and 50 s.

2.2 Phase identification

In RF data, the travel-times of the converted phases relative to the direct P arrival depend on the epicentral distance. This is generally seen as phase move-out which is different for direct and multiply converted phases, and helps to distinguish between these. For complex structures with dipping interfaces and seismic anisotropy, the travel-times and amplitudes of conversions also vary with back-azimuth. Although events generated from similar epicentral distance and back-azimuths should theoretically have coherent conversions and multiples, interference with scattered wave-field, small scale heterogeneity and random noise generates variations which can be seen as perturbations superimposed on the response of the primary sub-surface feature. The observed RF data matrix, $Y_{n \times p} = X_{n \times p} + \sigma Z_{n \times p}$,

can now be modelled as a fixed rank perturbation ($\text{rank}[X] = r \leq n$) of the random noise matrix $Z \sim \mathcal{N}(0, 1)$. This is known as the spiked covariance model (Johnstone, 2001). To extract an approximation of the uncontaminated response $\hat{X}(Y)_{n \times p} \approx X_{n \times p}$, we exploit the fact that the asymptotic eigenvalue distribution of the covariance of a random matrix follows the Marchenko-Pastur (MP) law (Marchenko & Pastur, 1967) which has a compact support Ω with bounds λ_{\pm}

$$p(\lambda|\sigma, \gamma) = \begin{cases} \frac{\sqrt{(\lambda_+ - \lambda)(\lambda - \lambda_-)}}{2\pi\lambda\gamma\sigma}, & \lambda_- \leq \lambda \leq \lambda_+ \\ 0, & \text{otherwise} \end{cases}, \text{ with } \lambda_{\pm} = \sigma^2(1 \pm \sqrt{\gamma})^2 \quad (1)$$

λ_- , λ_+ , σ , and γ denote the smallest eigenvalue, largest eigenvalue, noise level and matrix aspect ratio n/p , respectively. λ_{\pm} fluctuate on the small scale $n^{-2/3}$ according to the Tracy-Widom distribution (Tracy & Widom, 1996). Qualitatively, the empirical distribution of the eigenvalues of Z forms a deformed quarter circle bulk with bulk edges given by λ_{\pm} and bulk width $4\sqrt{\gamma}\sigma^2$, and all eigenvalues lie strictly within these bounds. The eigenvalues show a sort of self-arranging behaviour which, in presence of a non-random sample coherency (i.e., $X \neq 0$), have a repulsion effect on the signal eigenvalue if present. Thus we see a phase transition phenomenon (Baik et al., 2005) where, above a certain signal threshold, the signal eigenvalues separate away from the bulk "noise" eigenvalues and converge asymptotically to a different distribution. The same follows for the singular values which scale as the square root of the eigenvalues (Benaych-Georges & Nadakuditi, 2012). Setting $X_n = \sum_{i=1}^p a_{n,i}x_i b_{n,i}^T$ and $Y_n = \sum_{i=1}^p u_{n,i}y_i v_{n,i}^T$, the BBP (Baik-Ben Arous-Péché) phase transition results in a mapping of singular values y_i of the observed matrix Y to x_i of the uncontaminated low rank signal X :

$$y_i \xrightarrow{\text{a.s.}} \begin{cases} \sigma(1 + \sqrt{\gamma}) & x_i \leq \sigma\gamma^{\frac{1}{4}} \\ \sqrt{(x_i + \frac{\sigma}{x_i})(x_i + \gamma\frac{\sigma}{x_i})}, & x_i > \sigma\gamma^{\frac{1}{4}} \end{cases} \quad (2)$$

Similarly, the left and right singular vectors pairs (u_i, a_i) and (v_i, b_i) are orthogonal within the bulk but become strongly correlated and show a non-zero dot product past the critical point:

$$|\langle a_{n,i}, u_{n,j} \rangle|^2 \xrightarrow{\text{a.s.}} \begin{cases} \frac{x_i^4 - \gamma}{x_i^4 + \gamma x_i^2}, & x_i = x_j \\ 0, & x_i \neq x_j \end{cases} \quad (3)$$

$$|\langle b_{n,i}, v_{n,j} \rangle|^2 \xrightarrow{\text{a.s.}} \begin{cases} \frac{x_i^4 - \gamma}{x_i^4 + x_i^2}, & x_i = x_j \\ 0, & x_i \neq x_j \end{cases} \quad (4)$$

Using these transition equations, Gavish & Donoho (2014) derive an analytical expression for the optimal rank- r approximation of the data matrix $\hat{X}(Y)$ by minimising the asymptotic mean squared error of their misfit $\|X - \hat{X}(Y)\|_F^2$ over all singular values $u_i > \sigma\sqrt{1 + \gamma}$ and $0 < \gamma \leq 1$. This results in an expression for a threshold value τ

$$\tau = \lambda_{\star}(\gamma) \cdot \sqrt{n}\sigma \quad (5)$$

where

$$\lambda_{\star} = \sqrt{(2\gamma + 1) + \frac{8\gamma}{(\gamma + 1) + \sqrt{(\gamma^2 + 14\gamma + 1)}}} \quad (6)$$

This threshold marks the unique transition point of the signal singular values from those of random noise matrix Z for a given spectral distribution of Y with noise σ , taking into account the support fluctuations. The median of a standard MP distribution ($\sigma = 1$) is given by

$$\mu_{MP} = \frac{1}{2\pi t} \int_{\lambda_-}^x \sqrt{(\lambda_+ - t)(t - \lambda_-)} dt \quad (7)$$

The noise σ can be estimated by matching the median of the standard MP distribution to that of the bulk singular values. This results in a robust noise estimator that estimates noise by comparing the perturbed singular values with the MP distribution

$$\hat{\sigma}(Y) := \frac{\lambda_{med}}{\sqrt{n\mu_{MP}}} \quad (8)$$

Using $\hat{\sigma}(Y)$ for σ in eq. 5, we get

$$\hat{\tau}_* = \omega(\gamma) \cdot y_{med} \quad (8)$$

where

$$\omega(\gamma) \approx 0.56\gamma^3 - 0.95\gamma^2 + 1.82\beta + 1.43 \quad (9)$$

In the final step, the singular value matrix y_i is replaced by \hat{y}_i where the values below the threshold limit given by eq. 5 are padded and the approximate uncontaminated signal matrix $\hat{X}(Y)$ is reconstructed from the observations Y using $\hat{X}(Y) = \sum_{i=1}^p u_{n,i} \hat{y}_i v_{n,i}^T$. In essence, the outlined procedure provides objective criteria to select the number of principal components that describe the variance of the structural signal by modelling noise as an additive independent and identically distributed (i.i.d.) random matrix.

2.3 Apparent velocity curves

In order to reduce non-uniqueness in the inversion of receiver functions, we make use of the absolute S-wave velocity information contained within the P-wave polarization as a complementary constraint. A consequence of Snell's law, the relation between the apparent P-wave incidence angle (\bar{i}_p) and the subsurface S-wave velocity was derived by Wiechert (1907) and is given by eq. 10. Here p denotes the ray parameter. This apparent P-wave incidence angle can be calculated directly from the amplitudes of vertical and radial receiver functions at time $t=0$, as described in Svenningsen & Jacobsen (2007)

$$v_{S,app} = \sin(0.5\bar{i}_p)/p \quad (10)$$

$$\tan \bar{i}_p = \frac{RRF(t=0)}{ZRF(t=0)} \quad (11)$$

Following a similar procedure as Knapmeyer-Endrun et al. (2018) and estimating i_p as a function of low pass Butterworth filter period (T), we calculate a frequency-dependent S-wave velocity curve $v_S(T)$ which emphasises the absolute S-wave velocity variation with depth. A mean RF is calculated from all the raw RF waveforms in the dataset. This is then used to compute a $v_{S,app}$ curve which is jointly inverted together with the mean RF. We measure the dominant period of the spike in the mean ZRF and discard the values of filter periods smaller than that.

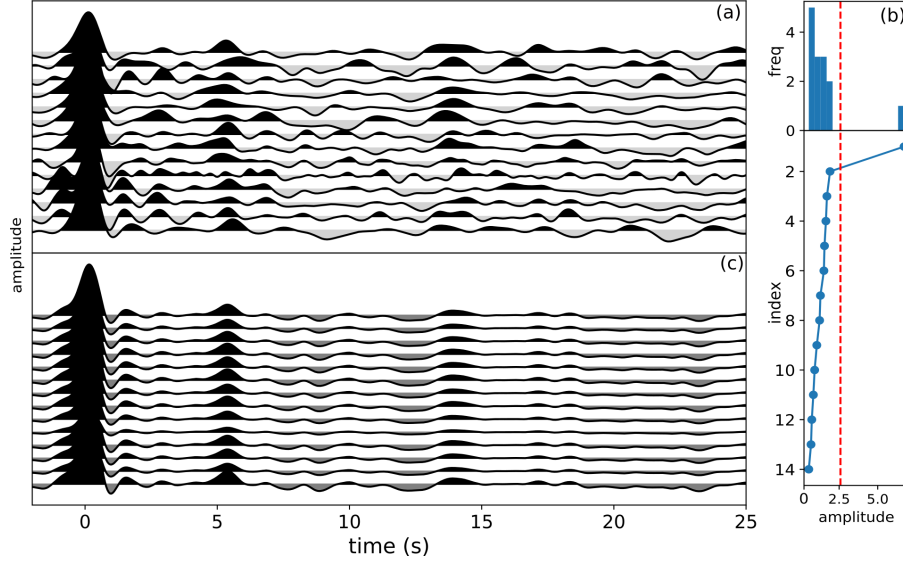


Figure 1. (a) Raw RFs from terrestrial station VSU in epicentral distance range $65^\circ - 69^\circ$ and back-azimuth $10^\circ - 40^\circ$ (b) distribution of the singular spectrum (top) and the singular values arranged in decreasing amplitude (below). The red dashed line denoted the noise threshold. (c) RFs reconstructed using singular values above noise threshold. The epicentral distance increases from top to bottom in (a) and (c).

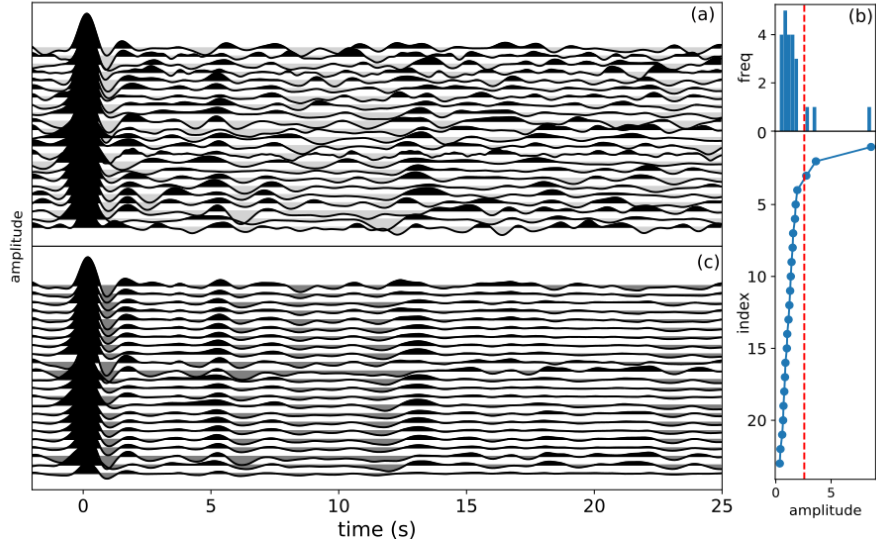


Figure 2. Same as Figure 1 but for epicentral distance range $55^\circ - 85^\circ$ and back-azimuth between $80^\circ - 120^\circ$. The epicentral distance increases from top to bottom.

2.4 Inversion

A Markov-chain Monte Carlo (McMC) transdimensional Bayesian inversion method based on Bodin et al. (2012) (Dreiling & Tilmann, 2019) was used for the joint inversion of

the mean RF and $v_{S,app}$ curve. In this formulation, the number of layers itself becomes an unknown and is also inverted for along with the other model parameters. The solution is an ensemble of models that are distributed according to a posterior probability density function given by Bayes’s rule. Each layer is parameterised by depth, V_s and the v_P/v_S ratio. Density is not inverted for but is calculated using the Birch law (Birch, 1961). We use flat model priors and their ranges for depth, V_s and v_P/v_S ratio were set to 0 – 100 km, 1 – 5 km/s and 1.4 – 2.2, respectively. A maximum of 20 layers was imposed and the range for noise amplitude was set to 0.01 – 0.5 with correlation values of RF and $v_{S,app}$ data fixed to 0.96 and 0, respectively. For calculating synthetic RFs, we use the forward calculation module implemented by Shibutani et al. (1996). The algorithm calculates the impulse response of a layer stack in the P-SV system. The resulting synthetic Z- and RRFs are convolved with the observed ZRF in order to account for the observed waveform complexity (Knapmeyer-Endrun et al., 2018). A $v_{S,app}$ profile is then calculated for the RFs using the procedure described in Section 2.3.

3 Results

To illustrate the method we show its application on data from the terrestrial seismic station VSU. The Figure 1(a) shows the raw data which consists of RFs computed from closely located events. In general the data are noisy. The subplot (b) shows the distribution of singular values and its spectrum for the data. We see the general singular value repulsion behaviour with a “bulk” noise region well separated away from the signal “spike”. This noise bulk follows the limiting spectral distribution given by the MP law with support values and variance given by Eq. 1 and 8. The red line shows the optimal threshold for singular value truncation when noise is modelled as an i.i.d. random matrix. Using the singular value lying above this threshold, we reconstruct the data by projecting it onto the corresponding eigenvector. Subplot (c) shows the reconstructed RF data showing clear coherent energy arrivals at $\sim 1, 5, 12$ and 14 and 23 s. We interpret these as the the intra-crustal, Moho Ps, a low velocity zone, PpPs and PpSs phases, respectively. The reference timing for the Moho Ps phase here is taken from Knapmeyer-Endrun et al. (2014). In general, the method is applicable equally well to data sets covering a wider range of distances and back-azimuths. The number of singular values above the threshold then increases to accommodate the data variance. In Figure 2 shows the reconstruction of RFs from similar back-azimuths but a wider epicentral distance range ($55^\circ - 85^\circ$). Here the threshold increases to three to accommodate the move-out of various phases.

Figure 3 shows the result of applying the phase identification methodology to our selected data from the InSight mission. Apart from the three primary phases at 2.4, 4.8, and 7.2 s previously identified in Knapmeyer-Endrun et al. (2021), the raw RF data (subplot(a)) does not seem to contain any consistent phases after the initial 8 s. From subplot (b), we see that the first principal component is sufficient to identify the main phase arrivals within the first 30s of the RF waveforms. This is expected as all the events considered here have similar distances and back-azimuths. The reconstructed RF waveforms are shown in subplot (c). In addition to the three primary phases, we report three new multiply reflected phases at 15, 20, and 23 s. We interpret these as the P_2pPs , P_2pSs and P_3pPs phases, where the sub-scripted numeral in the phase name denotes the generating interface. Note that the P_3pPs phase holds significant importance as it corroborates the existence of the much speculated third inter-crustal layer below the InSight landing site. A misfit function is calculated using these arrival timings using which the mean RF is jointly inverted with the mean $v_{S,app}$. We initialised 72 chains of 1,000,000 iterations, each sampling the model space simultaneously and independently, with 500,000 iterations discarded as the burn-in phase. Outlier chains were removed and the models were thinned to obtain a final ensemble of 100,000 models. The main results of the inversion are shown in Figure 4. A three-layer model exhibits the highest probability density in the solution ensemble. Subplot (a) shows the posterior distribution of the v_S profiles as a function of depth, along with the probability

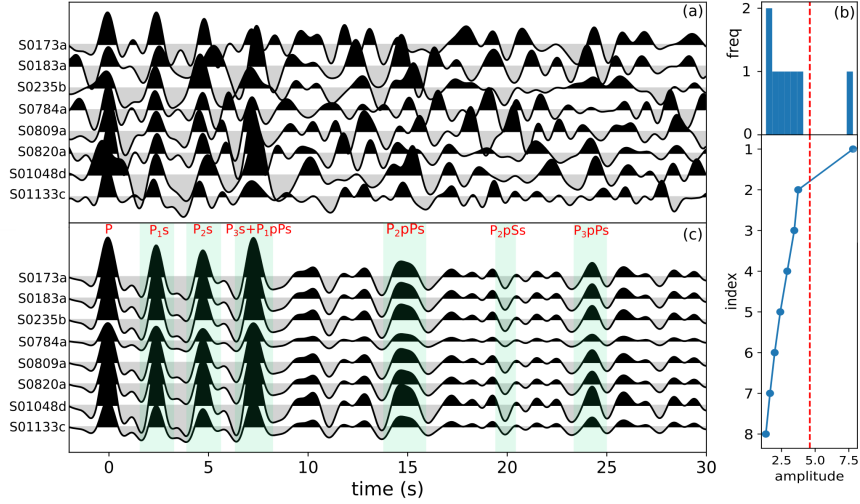


Figure 3. Same as Figure 1 but for Mars. The shaded regions show the denoted arrivals.

for each interface depth. We see two well-defined mid-crustal interfaces at depths of 8.5 ± 1.5 km and 22 ± 3 km, along with the crust-mantle transition at 43 ± 5 km. The resulting crustal models agree well with the three-layer models predicted in Knapmeyer-Endrun et al. (2021) and Durán et al. (2022). The modelled $v_{S,app}$ curves and the RFs follow the observed data closely and are shown in subplots (b) and (c), respectively. Due to the low SNR of the individual RF waveforms at longer periods, the $v_{S,app}$ curves are limited to periods < 14 s. This helps provide tight constraints on the observed v_S value within the shallow part of the crust but the uncertainty increases with depth where the v_S values and their increases are primarily controlled by the RF amplitudes. The estimated mean v_P/v_S ratio for the three layers is 1.81 ± 0.05 , 1.77 ± 0.06 and 1.64 ± 0.08 , yielding an average value of ~ 1.75 for the crust. A plot of the 1D distribution for v_S and v_P/v_S ratio for the models along with noise characteristics is provided in the supplementary materials. A distinct negative arrival of unclear origin is seen at 11.5 s. Although we do not include this in our analysis to avoid over-interpretation, it could either be a Pp phase from the second interface or a low-velocity zone at a depth of $\sim 70 - 75$ km. The P_1pPs would arrive earlier between 8-10 s, ruling out its possibility.

4 Discussion

With just a handful of good quality, small magnitude and closely located marsquakes, the analysis of the RF data from the Insight mission present us with many challenges. In this work, we attempt to use this close distance range to our advantage to uncover additional features in the data using concepts of random matrix theory and principal component analysis. For events from similar distances and back-azimuths, considerably fewer principal components are needed as distance and back-azimuth ranges increase. Using synthetics and real data, Zhang et al. (2019) demonstrated that just the first few principal components could effectively reconstruct all the data variance within events from varying back-azimuths. Here we used events with varying distances and similar back-azimuths to establish an equivalent idea. A few points are, however, worth noting. Occasionally, data reconstruction with a few principal components can lead to an erroneous broadening of phases. Though it does not affect the detection of phases, it could sometimes lead to an unwanted merger of very close arrivals. We also find that the singular spectrum, and hence the resulting threshold, can

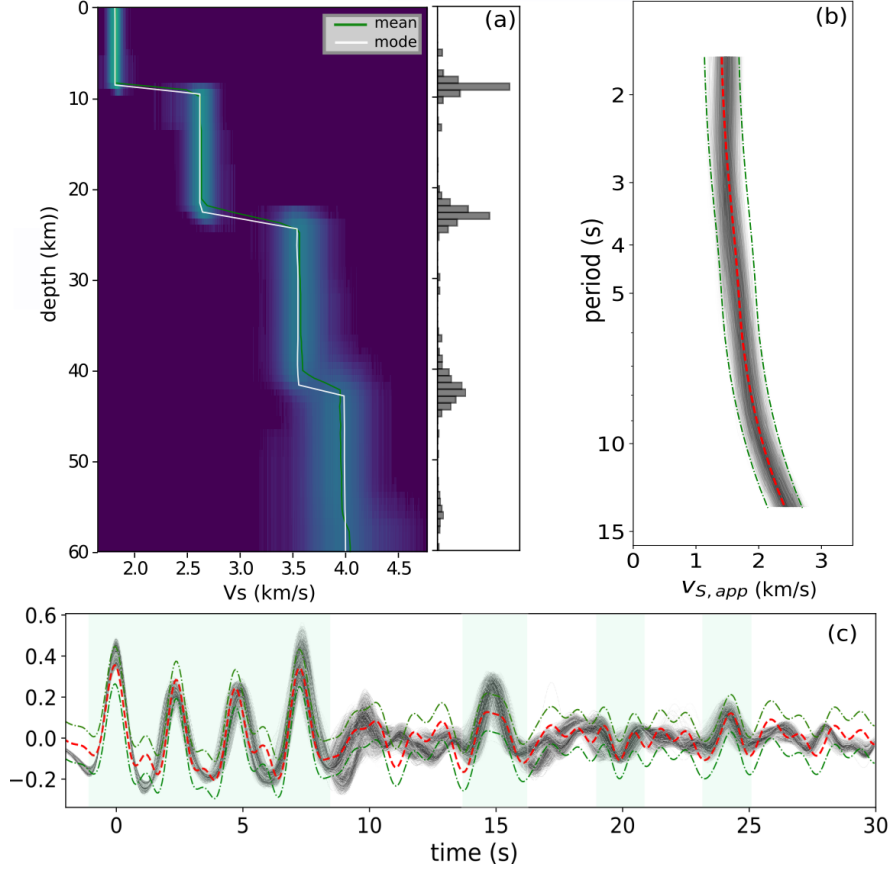


Figure 4. (a) Posterior density of resulting Vs profiles along with histograms for interface depth (b) Fit to the mean $v_{S,app}$ curve (c) Fit to the mean RF waveform. The red dashed lines denotes the observed data and green dash-dotted lines represent the 2σ uncertainty.

show slight variations based on the dataset’s quality. For highly irregular RF waveforms, this could severely bias the threshold estimate to lower values. In this case, utilising higher principal components for data reconstruction will likely result in individual waveform variations instead of emerging features like phase move-out and back-azimuth variations. We recommend removing such outlier waveforms before the analysis. The compact support of the random singular values can sometimes be disconnected, and therefore, choosing the threshold based only visually on the histograms can lead to errors. On the other hand, histogram bins might not always clearly reflect the transition gap from random to signal singular values. A full computation of the threshold is therefore required. An inspection of the data covariance matrix can often reveal how well the data follows the spiked covariance model and can provide extra insight into the validity of the assumptions for the particular dataset. The number of events is also an essential factor. As the size of the dataset (m,n) increases, the fluctuations of the Tracy-Widom distribution decrease. Thus, the larger the dataset, the higher the stability of the threshold. For a small dataset, the assumption of the spiked covariance model can break down. Finally, the noise in receiver functions is not entirely random and generally has a finite covariance. A recent study by Donoho et al. (2020) generalises the spiked covariance model to include correlated noise. We performed further tests with the new method, and although the variations were not significant, it seemed to affect more the case with events from a larger distance range. The results remained unchanged for events within close distances like the InSight with a slight

increment in the threshold value. Extending this analysis to include the correlated case is nevertheless essential and will be the subject of a later study.

5 Summary and Conclusion

The receiver function method has played an instrumental role in the analysis of the Martian crustal structure using data from the InSight mission. In order to contribute to that effort, here we present a method to identify coherent phase arrivals in noisy RF waveforms by modelling data noise as samples from an i.i.d random matrix and using this information to jointly invert the RFs with apparent velocity curves. With examples from terrestrial data, we first show how only a few singular values can help reconstruct coherent parts of the signals enabling the detection of phase arrivals in RF waveforms. The number of singular values needed for this depends on the range of the distance and back-azimuths of the events in the dataset, with often a single value being sufficient in the special case of closely located events. We then apply this method to a set of 8 marsquakes detected by the InSight mission and evaluate the crustal structure below the landing site based on these data. Three new crustal phases were identified in the RF waveforms, which we interpret as P₂pPs, P₂pSs and P₃pPs phases. A subsequent joint inversion of the RFs with the mean $v_{S,app}$ curve shows that the crust of Mars below the InSight landing site is composed of three distinct layers with increasing velocity. A crustal thickness of ~ 43 km is estimated. The results are in agreement with previous work from Knapmeyer-Endrun et al. (2021), with the new P₃pPs phase suggesting a strong preference for the three-layer model in their study. A variety of interpretations are available for the existence of the first two interfaces ranging from a change in porosity to chemical composition. The preferred interpretation from Wieczorek et al. (2022) considers this a result of a series of transitions from sediments or pyroclastic deposits that experienced aqueous alterations to less porous Utopia ejecta and finally to the pre-existing crustal materials from early differentiation of Borealis impact melt. A thicker crust, like one obtained from such a three-layer model, is also more compatible with the amount of heat-producing elements within the Martian crust estimated by spectroscopy observations (Taylor, 2013; Knapmeyer-Endrun et al., 2021) and geodynamical modelling. A much lower bulk crustal density and significant enrichment in crustal heat-producing elements would otherwise be needed for a thinner crust (Knapmeyer-Endrun et al., 2021). However, it is unlikely that this three layered formation is indicative of the global Martian crustal structure which is known to have large lateral variations (Wieczorek et al., 2022), and can be plausibly just a feature of the local geology in the vicinity of the InSight landing site

Acknowledgments

R.J. acknowledges the funding provided by the IMPRS and the Emeritus group. The MPS MPG SEIS team acknowledges funding for development of the SEIS leveling system by the DLR German Space Agency. We acknowledge NASA, CNES, their partner agencies and Institutions (UKSA, SSO, DLR, JPL, IPGP-CNRS, ETHZ, IC, MPS-MPG) and the flight operations team at JPL, SISMOC, MSDS, IRIS-DMC and PDS for providing SEED SEIS data. This paper is InSight Contribution Number 188.

Open Research

Seismic data for station VSU are publically available and can be obtained from EIDA (<http://eida.gfz-potsdam.de/webdc3/>) using the event information provided in the supplementary material. The InSight seismic data presented here (<http://dx.doi.org/10.18715/SEIS.INSIGHT.XB.2016>) are publicly available through the Planetary Data System (PDS) Geosciences node of the Incorporated Research Institutions for Seismology (IRIS) Data Management Center under network code XB (<https://pds-geosciences.wustl.edu/missions/insight/seis.htm>), and through the data center of Institut de Physique du Globe, Paris (<http://seis-insight.eu>).

References

- Ammon, C. J. (1991). The isolation of receiver effects from teleseismic P waveforms. *Bull. of the Seism. Soc. Am.*, *81*, 2504-2510.
- Baik, J., Arous, G. B., & Péché, S. (2005). Phase transition of the largest eigenvalue for nonnull complex sample covariance matrices. *The Annals of Probability*, *33*(5), 1643–1697.
- Banerdt, W. B., Smrekar, S. E., Banfield, D., Giardini, D., Golombek, M., Johnson, C. L., ... others (2020). Initial results from the insight mission on mars. *Nature Geoscience*, *13*(3), 183–189.
- Benaych-Georges, F., & Nadakuditi, R. R. (2012). The singular values and vectors of low rank perturbations of large rectangular random matrices. *Journal of Multivariate Analysis*, *111*, 120–135.
- Birch, F. (1961). The velocities of compressional waves in rocks to 10 kilobars, Part 2. *J. Geophys. Res.*, *66*, 2199-2224.
- Bodin, T., Sambridge, M., Tkalčić, H., Arroucau, P., Gallagher, K., & Rawlinson, N. (2012). Transdimensional inversion of receiver functions and surface wave dispersion. *Journal of Geophysical Research: Solid Earth*, *117*(B2).
- Clinton, J. F., Ceylan, S., van Driel, M., Giardini, D., Stähler, S. C., Böse, M., ... others (2021). The Marsquake catalogue from InSight, sols 0–478. *Physics of the Earth and Planetary Interiors*, *310*, 106595.
- Compaire, N., Margerin, L., Garcia, R. F., Pinot, B., Calvet, M., Orhand-Mainsant, G., ... others (2021). Autocorrelation of the ground vibrations recorded by the SEIS-InSight seismometer on mars. *Journal of Geophysical Research: Planets*, *126*(4), e2020JE006498.
- Donoho, D. L., Gavish, M., & Romanov, E. (2020). ScreeNOT: Exact MSE-optimal singular value thresholding in correlated noise. *arXiv preprint arXiv:2009.12297*.
- Dreiling, J., & Tilmann, F. (2019). BayHunter-McMC transdimensional Bayesian inversion of receiver functions and surface wave dispersion.
- Drilleau, M., Samuel, H., Garcia, R. F., Rivoldini, A., Perrin, C., Michaut, C., ... et al. (2022). Marsquake locations and 1-d seismic models for mars from insight data. *Earth and Space Science Open Archive*, *77*. doi: 10.1002/essoar.10511074.2
- Du, Z., & Foulger, G. (1999). The crustal structure beneath the northwest fjords, Iceland, from receiver functions and surface waves. *Geophysical Journal International*, *139*(2), 419–432.
- Durán, C., Khan, A., Ceylan, S., Zenhäusern, G., Stähler, S., Clinton, J., & Giardini, D. (2022). Seismology on Mars: An analysis of direct, reflected, and converted seismic body waves with implications for interior structure. *Physics of the Earth and Planetary Interiors*, *325*, 106851.
- Gagnepain-Beyneix, J., Lognonné, P., Chenet, H., Lombardi, D., & Spohn, T. (2006). A seismic model of the lunar mantle and constraints on temperature and mineralogy. *Physics of the Earth and Planetary Interiors*, *159*(3-4), 140–166.
- Gavish, M., & Donoho, D. L. (2014). The optimal hard threshold for singular values is $4/\sqrt{3}$. *IEEE Transactions on Information Theory*, *60*(8), 5040–5053.
- Giardini, D., Lognonné, P., Banerdt, W. B., Pike, W. T., Christensen, U., Ceylan, S., ... others (2020). The seismicity of Mars. *Nature Geoscience*, *13*(3), 205–212.
- Hannemann, K., Krüger, F., Dahm, T., & Lange, D. (2017). Structure of the oceanic lithosphere and upper mantle north of the Gloria fault in the eastern mid-Atlantic by receiver function analysis. *J. Geophys. Res.*, *122*, 7927-7950. doi: 10.1002/2016JB013582
- InSight Mars SEIS Data Service. (2019). SEIS raw data, Insight Mission. *IPGP, JPL, CNES, ETHZ, ICL, MPS, ISAE-Supaero, LPG, MFSC*.
- InSight Marsquake Service. (2022). *Mars seismic catalogue, insight mission; v10 2022-04-01*. ETHZ, IPGP, JPL, ICL, Univ. Bristol. Retrieved from <https://www.insight.ethz.ch/seismicity/catalog/v10> doi: 10.12686/a16
- Johnstone, I. M. (2001). On the distribution of the largest eigenvalue in principal compo-

- nents analysis. *The Annals of statistics*, 29(2), 295–327.
- Joshi, R., Knapmeyer-Endrun, B., Mosegaard, K., Igel, H., & Christensen, U. R. (2021). Joint Inversion of Receiver Functions and Apparent Incidence Angles for Sparse Seismic Data. *Earth and Space Science*, 8(10), e2021EA001733. Retrieved from <https://agupubs.onlinelibrary.wiley.com/doi/abs/10.1029/2021EA001733> (e2021EA001733 2021EA001733) doi: <https://doi.org/10.1029/2021EA001733>
- Julia, J., Ammon, C. J., Herrmann, R., & Correig, A. M. (2000). Joint inversion of receiver function and surface wave dispersion observations. *Geophysical Journal International*, 143(1), 99–112.
- Khan, A., Ceylan, S., van Driel, M., Giardini, D., Lognonné, P., Samuel, H., ... others (2021). Upper mantle structure of mars from insight seismic data. *Science*, 373(6553), 434–438.
- Kim, D., Lekić, V., Irving, J. C. E., Schmerr, N., Knapmeyer-Endrun, B., Joshi, R., ... Banerdt, W. B. (2021). Improving Constraints on Planetary Interiors with PPs Receiver Functions. *Journal of Geophysical Research: Planets*, 126(11), e2021JE006983. Retrieved from <https://agupubs.onlinelibrary.wiley.com/doi/abs/10.1029/2021JE006983> (e2021JE006983 2021JE006983) doi: <https://doi.org/10.1029/2021JE006983>
- Knapmeyer-Endrun, B., Ceylan, S., & van Driel, M. (2018). Crustal S-wave velocity from apparent incidence angles: a case study in preparation for InSight. *Space Science Reviews*, 214(5), 83.
- Knapmeyer-Endrun, B., Krüger, F., & Group, t. P. W. (2014). Moho depth across the Trans-European Suture Zone from P-and S-receiver functions. *Geophysical Journal International*, 197(2), 1048–1075.
- Knapmeyer-Endrun, B., Panning, M. P., Bissig, F., Joshi, R., Khan, A., Kim, D., ... others (2021). Thickness and structure of the martian crust from InSight seismic data. *Science*, 373(6553), 438–443.
- Li, J., Beghein, C., Wookey, J., Davis, P., Lognonné, P., Schimmel, M., ... Banerdt, W. B. (2022). Evidence for crustal seismic anisotropy at the InSight lander site. *Earth and Planetary Science Letters*, 593, 117654.
- Lognonné, P., Banerdt, W. B., Giardini, D., Pike, W., Christensen, U., Laudet, P., ... others (2019). SEIS: InSight’s seismic experiment for internal structure of Mars. *Space Science Reviews*, 215(1), 12.
- Lognonné, P., Banerdt, W. B., Pike, W., Giardini, D., Christensen, U., Garcia, R. F., ... others (2020). Constraints on the shallow elastic and anelastic structure of mars from insight seismic data. *Nature Geoscience*, 13(3), 213–220.
- Lognonné, P., Gagnepain-Beyneix, J., & Chenet, H. (2003). A new seismic model of the Moon: implications for structure, thermal evolution and formation of the Moon. *Earth and Planetary Science Letters*, 211(1-2), 27–44.
- Marchenko, V. A., & Pastur, L. A. (1967). Distribution of eigenvalues for some sets of random matrices. *Matematicheskii Sbornik*, 114(4), 507–536.
- Schimmel, M., Stutzmann, E., Lognonné, P., Compaire, N., Davis, P., Drilleau, M., ... others (2021). Seismic noise autocorrelations on Mars. *Earth and Space Science*, 8(6), e2021EA001755.
- Shibutani, T., Sambridge, M., & Kennett, B. (1996). Genetic algorithm inversion for receiver functions with application to crust and uppermost mantle structure beneath eastern Australia. *Geophys. Res. Lett.*, 23, 1829–1832. doi: [doi:10.1029/96GL01671](https://doi.org/10.1029/96GL01671)
- Svenningsen, L., & Jacobsen, B. (2007). Absolute S-velocity estimation from receiver functions. *Geophysical Journal International*, 170(3), 1089–1094.
- Taylor, G. J. (2013). The bulk composition of Mars. *Geochemistry*, 73(4), 401–420.
- Tracy, C. A., & Widom, H. (1996). On orthogonal and symplectic matrix ensembles. *Communications in Mathematical Physics*, 177(3), 727–754.
- Vinnik, L., Chenet, H., Gagnepain-Beyneix, J., & Lognonne, P. (2001). First seismic receiver functions on the Moon. *Geophysical research letters*, 28(15), 3031–3034.

- Wiechert, E. (1907). Über Erdbebenwellen. I. Theoretisches über die Ausbreitung der Erdbebenwellen. *Nachrichten von der Gesellschaft der Wissenschaften zu Göttingen, Mathematisch-Physikalische Klasse*, 415-429.
- Wieczorek, M. A., Broquet, A., McLennan, S. M., Rivoldini, A., Golombek, M., Antonangeli, D., ... others (2022). InSight constraints on the global character of the Martian crust. *Journal of Geophysical Research: Planets*, e2022JE007298.
- Zhang, J., Chen, L., & Wang, X. (2019). Crustal structure study based on principal component analysis of receiver functions. *Science China Earth Sciences*, 62(7), 1110–1124.